

Flexible Capacitive Curvature Sensor with One-Time Calibration for Amphibious Gait Monitoring

Xin Li,¹ Jiajie Guo,¹ Xingxing Ma,¹ Luye Yang,¹ Kok-Meng Lee,² and Caihua Xiong¹

Abstract

Wearable devices developed with flexible electronics have great potential applications for human health monitoring and motion sensing. Although material softness and structural flexibility provide a deformable human–machine interface to adapt to joint bending or tissue stretching/compression, flexible sensors are inconvenient in practical uses as they usually require calibration every time they are installed. This article presents an approach to design and fabricate a flexible curvature sensor to measure human articular movements for amphibious applications. This flexible sensor employs the capacitive sensing principle, where the dielectric layer and electrodes are made from the polyurethane resin and eutectic gallium-indium (EGaIn) liquid metal; and the fabrication process is implemented with shape deposition molding for batch production. The sensing method for articular rotation angles employs the Euler beam model to make the sensor reusable after one-time calibration by compensating for the unpredicted manual installation error. The illustrative application to ankle sensing in amphibious gaits shows that the root-mean-square error is within 5° for different walking speeds (0.7–1.1 m/s) in treadmill tests and the maximum error is within 3° for underwater sensing with quasi-static measurements. It is expected that the proposed waterproof flexible sensor can push the boundaries of wearable robotics, human locomotion, as well as their related applications.

Keywords: flexible curvature sensor, wearable device, amphibious measurement, capacitance, one-time calibration

Introduction

FLexible sensors have attracted growing interests in recent years for applications in human motions monitoring,^{1–10} soft robotics,^{11–13} human–machine interaction^{5,11,14,15} and physiology monitoring.^{7,16–18} Although motion capture systems^{10,19} or medical equipment²⁰ provide promising ways for measuring limb motions and muscle states, they are limited to controlled environments and professional protocols. Aiming at developing wearable robotics for ease of motion sensing under harsh conditions, this article proposes a flexible sensor capable of repetitive uses with one-time calibration for both on-land and underwater measurements.

Applications of flexible strain sensors are usually illustrated by capturing articular joint rotations^{1,21,22} or soft tissue deformations^{7,23} through strains due to elongation, com-

pression, or bending. Perfect adhesion between a sensor and human body is necessary for strain sensing, so the sensors have to be conformal to natural anatomical surfaces and adaptable to nonlinear strains. In this way, attachment techniques are needed such as the sticky elastomer to human skins²⁴ and the hook-and-loop to a generic clothing.²¹ However, practical issues such as drastic motions, moisture/dusty environments, and repetitive uses could loosen sensor attachment and deteriorate sensing precision. Also, it is still lack of in-depth knowledge of microscale mechanics behind the strain-responsive behaviors of flexible sensors,²⁵ which renders challenges in establishing computational models and numerical methods for sensor calibration in practice. For example, recalibration is required every time a strain sensor is applied to measure human joint motions, because the non-linear relation between measured strain and rotation angle

¹State Key Laboratory of Digital Manufacturing Equipment and Technology, School of Mechanical Science and Engineering, Huazhong University of Science and Technology, Wuhan, Hubei, China.

²George W. Woodruff School of Mechanical Engineering, Georgia Institute of Technology, Atlanta, Georgia, USA.

changes with preloading and dislocation during sensor installation.

Compared with the fruitful research on strain sensors, there are few reports on measuring bending deformations with curvature sensors. In fact, curvature sensing relaxes the rigid bonding requirement of strain sensing by allowing for sensor slippage on a human body. Also, existing theoretical models for compliant mechanism deflection provide a good fundamental for calibration of curvature sensors. Among the scant available literatures on curvature sensors, the nondifferential mechanism was designed in a soft microfluidic film for direct curvature sensing²⁶; however, the root-mean-square (RMS) error of the sensor is $>7.9^\circ$, which is not satisfactory for application of human–exoskeleton interaction. Recently, the curvature sensor integrated with flexible electronics was developed for monitoring joint bending and body gestures,²⁷ illustrating the advantages of adhesion-free curvature measurements. However, few results have been reported on sensor calibration and performance in harsh environments for robotic applications.

Both curvature and strain sensors can be categorized into resistive^{9,21,24,25,28–40} and capacitive^{1,3,40–45} types. Resistive sensors exhibit high sensitivity with the gauge factor (GF) exceeding 1000³⁴ or even reaching 2000³³; however, nonlinearity in resistance would seriously weaken the sensing precision.¹⁶ Good applications of resistive sensors include motion pattern recognition and sign language understanding.⁴⁶ In contrast, although capacitive sensors have the maximum GF limited to one at the best effort,^{3,44} they embody excellent linearity to guarantee sensing precision.^{1,3,45} Besides, capacitive sensors excel resistive ones with better dynamic performance in terms of lower hysteresis⁴⁵ and smaller overshoot.^{3,9} It has been demonstrated that nonlinear responses in capacitive sensors can be avoided by appropriately adjusting the excitation frequency.⁴⁷ In both types of sensors, it is crucial to adapt to large tensions or compressions with a stretchable or bendable conductor, the manufacture of which has attempted various materials, including silver nanowires (AgNWs),^{4,28,31,45,48} liquid metals,^{21,24,39} carbon nanotubes,^{3,9,25,35,40,44} graphene^{32,34} and synthetic conductive inks.^{38,43} Among them, the gallium-based liquid alloy is a popular candidate because of its high electrical/thermal conductivity, extreme fluidity, and simple processing requirements.^{23,24,49} Elastomers for sensor infrastructures are usually based on silicone-like polydimethylsiloxane (PDMS)^{28,30,35,36,50} and Ecoflex^{25,38,40,45} that have good chemical inertness and small elastic modulus. Polyurethane with a much higher dielectric constant than siloxanes offers the optimal choice for the design of flexible capacitive sensors.¹⁵ It is noted that most capacitive sensors have been developed for strain sensing, and few capacitive curvature ones can be found.

In human motion monitoring, it is difficult to calibrate flexible sensor signals with joint rotation angles due to nonlinear musculoskeletal deformations and inconsistent sensor installation.^{1,9,28,32,38,43,45} The strain sensors on a bioinspired ankle-foot exoskeleton were calibrated with the inertial measurement units, where the mean error of the strain-derived joint angle was $0.3^\circ \pm 1.6^\circ$ with the maximum error of 4.3° .³⁹ Calibrated with the optical motion capture system, the soft sensing suit achieved RMS errors of $<5^\circ$ for the walking speed of 0.89 m/s and reached the maximum RMS error of 15° for the running

speed of 2.7 m/s.²¹ However, the aforementioned sensing systems are vulnerable to data drifts and installation errors that require recalibration from time to time. More recently, deep neural networks have been developed to map soft sensor signals to virtual states for human–machine interaction.⁵¹

In contrast, research on human motion monitoring mainly focuses on terrestrial gaits, and few sensor prototypes have been developed for underwater applications. Among the attractive topics in underwater sensing are waterproof sealing of electronic components and environmental effects on sensing precision. The roller coating method was demonstrated to encapsulate gold nanowire sensors and achieve water resistibility and durability.²⁹ The waterproof strain sensor was first developed with PDMS shielding.⁵⁰ As compared with PDMS that has disadvantages due to its aging effects, Ecoflex with water resistivity is a more environmentally stable polymer²⁵ and thus becomes a good candidate for sensor protection under water. Recently, the resistive strain sensor was mounted on a toy fish to measure tail swing in real time,⁵² and the waterproof triboelectric nanogenerator was developed as self-powered sensors.⁶ In the application of amphibious gait monitoring where underwater equipment are worn on human bodies, manual installation seriously affects the sensing model of a flexible sensor.

It is desired to achieve one-time calibration that is accomplished by accounting for the dominant effect of manual installation on repetitive uses of flexible sensors. Hence, the design and modeling method is proposed for the calibration purpose instead of a long product life. To achieve one-time calibration and sensing robustness for flexible sensors in harsh environments, this article proposes a capacitive curvature sensor for amphibious gait measurement where the design concept, fabrication process, sensor calibration and characterization, as well as illustrative application will be presented. It is expected that the proposed underwater flexible sensor can push the boundaries of wearable robotics, locomotion biomechanics, as well as their related applications.

Sensing Principle and Fabrication Method

Design concept

The sensing method is developed to relate the sensor bending angle with the capacitance change through the deformation curvature, and the sensing model is formulated for one-time calibration. Figure 1a shows the overview of the sensing system integrating the flexible capacitive module and data acquisition circuit, which can be mounted on a limb joint with bandages. The flexible capacitive sensor measures joint rotations through its bending curvature by deforming the parallel-plate capacitor as shown in Figure 1b, where two electrode plates, individually connected to the circuit board with a copper wire, are embedded in polyurethane resin elastomer. Overall dimensions of the sensing module are given by the length (L), width (W), and thickness (D) of the effective sensing module; and the step-shaped sections on both ends are designed for clamping and positioning.

To guarantee the effective capacitance is solely determined by the dimension of one electrode plate under bending deformations, the upper plate is slightly smaller than the bottom one ($w_1 < w_2$ and $l_1 < l_2$). In this way, the opposite area between the two electrode plates depends on the upper smaller one ($L_1 \times W_1$) during deformations (Fig. 1c). The

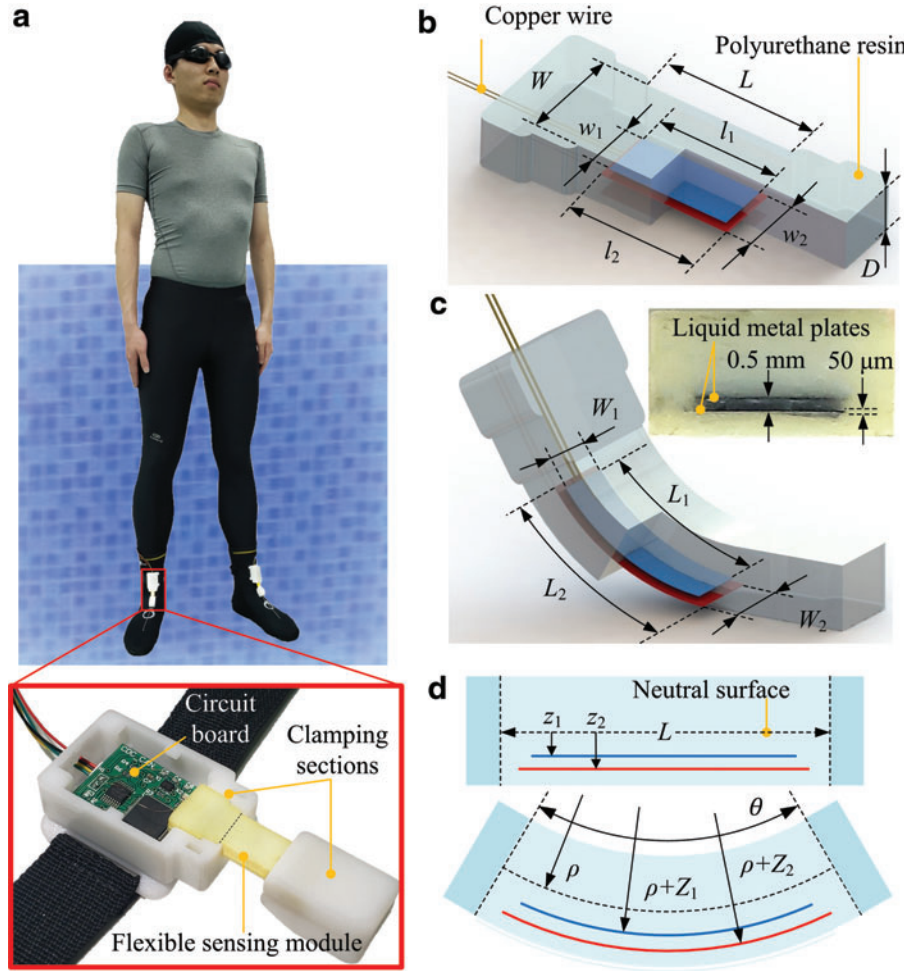


FIG. 1. Design concept of the capacitive curvature sensor. **(a)** Overview of the flexible capacitive sensing system. **(b)** Undeformed configuration of the curvature sensor. **(c)** Deformed configuration and cross-sectional view. **(d)** Schematic bending deformation of the curvature sensor. Color images are available online.

embedded photo shows that the thicknesses of the electrode plates and dielectric layer are 50 μm and 0.5 mm, respectively. Both electrodes lie on the same side of the neutral surface as depicted in Figure 1d, where θ is the bending angle of the flexible sensor; ρ is the radius of the neutral surface curvature; z_1 and z_2 (or Z_1 and Z_2) denote the distances from the upper and lower plates to the neutral surface without (or with) bending, respectively.

To establish the sensing model for joint rotation with the change of capacitance, the initial and deformed configurations of the sensor are modeled as parallel-plate and cylindrical capacitors, respectively,

$$C_0 = \frac{\epsilon_0 \epsilon_r l_1 w_1}{z_2 - z_1} \quad (1)$$

$$C = \frac{\kappa \epsilon_0 \epsilon_r l_1 W_1}{\ln \left(\frac{\rho + Z_2}{\rho + Z_1} \right)}, \quad (2)$$

where ϵ_r is the material dielectric constant and ϵ_0 is the dielectric constant in vacuum. On the basis of $z_2 - z_1 \ll l_1$ and $z_2 - z_1 \ll w_1$, the fringe field is assumed to be negligible. Since the effective elastomer is short, the bent shape of the

sensor under large deformation is approximated as a circular arc and the bending curvature is

$$\kappa = \frac{M}{EI}, \quad (3)$$

where M is the applied moment for bending, E is the elastic modulus, and I is the moment of inertia.

Employing the Euler beam theory that assumes cross sections remain planar and normal to the neutral surface,^{22,53} normal strains along the axial and lateral directions are obtained as linear functions of the distance z from the neutral surface

$$\varepsilon_a = \kappa z, \quad \varepsilon_l = -\nu \kappa z, \quad (4a, 4b)$$

where ν is the Poisson ratio. W_1 , Z_1 , and Z_2 are estimated by

$$W_1 = w_1(1 - \nu \kappa z_1) \quad (5a)$$

$$Z_1 = z_1(1 - \nu \kappa z_1) \quad (5b)$$

$$Z_2 = z_2(1 - \nu \kappa z_2). \quad (5c)$$

Substituting Equation (5) into Equation (2) gives

$$C = \kappa \varepsilon_0 \varepsilon_r w_1 l_1 \frac{1 - \nu \kappa z_1}{\ln \left[\frac{1 + \kappa z_2 (1 - \nu \kappa z_2)}{1 + \kappa z_1 (1 - \nu \kappa z_1)} \right]}. \quad (6)$$

Employing the Taylor's expansion at $\kappa=0$, Equation (6) is rewritten as

$$C/C_0 = 1 + b \cdot \kappa L + a \cdot (\kappa L)^2 + O(\kappa^3 L^3), \quad (7)$$

$$\text{where } a = \frac{(1+2\nu)(z_1+z_2)b}{2L} \text{ and } b = \frac{z_1+(1+2\nu)z_2}{2L} \quad (8a, 8b)$$

Neglecting the higher order terms and considering $\theta=\kappa L$, Equation (7) can be further simplified as

$$C/C_0 = a \cdot \theta^2 + b \cdot \theta + 1. \quad (9)$$

In practice, the coefficients a and b are not estimated from Equation (8) but calibrated with experimental data of C/C_0 and θ , because the structural dimensions and material property are affected by the fabrication and measurement processes. The bending angle θ is solved from the quadratic relation of Equation (9) with only one positive solution because both a and b are positive by the definitions in Equation (8). It is noted that θ represents the absolute rotation angle from the referenced state of undeformed sensor configura-

tion, so the calibrated sensing model is not affected by sensor installation thus can be used when the sensor is doffed and donned on again.

Sensor fabrication

The fabricating process of the flexible sensor with shape deposition molding (SDM) is illustrated in Figure 2 and Supplementary Video S1. The PU8400 (Hei-cast, Japan) solution, prepared with the uniformly mixed solution components in the equal weight ratio of 1:1:1, was cured into polyurethane elastomer in the wax mold container. Forming containers for molding each elastomer layer in the capacitive sensor, wax mold base, and covers were milling machined with different depths according to predesigned layer thicknesses. The depths of the mold base and covers (A, B, and C) were 2.5, 1, 1.5, and 2.5 mm, respectively. Geometric features were created in the mold covers for accommodating electrode plates and wires. Each cover can be positioned on the mold base with alignment pins in assembly. After the elastomer was cured and the wax cover A was removed, the copper conducting wire A was attached to the elastomer surface with the super glue (502 Deli, China), and the wire lacquer and redundant glue at the inserted end were removed with sand paper for optimal conduction.

The eutectic gallium-indium (EGaIn) liquid metal was sprayed on the elastomer to form electrode plates whose rectangular shapes were achieved with the three-dimensional

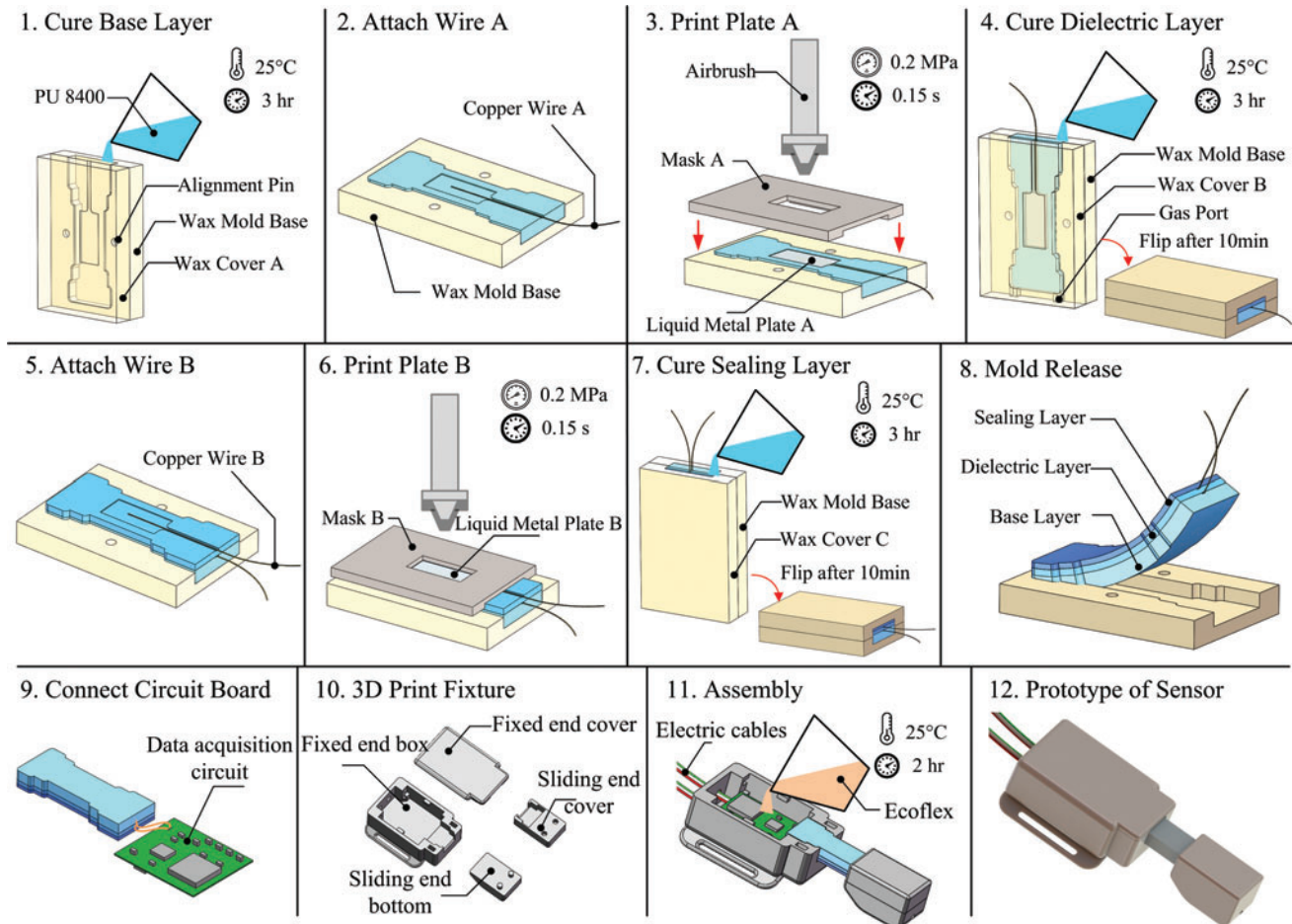


FIG. 2. Fabrication process of the flexible sensor (Supplementary Video S1). Color images are available online.

(3D)-printed resin masks. The printing process was performed on a 3D translation-motion platform that controls the position of the airbrush (PULEIPU, China), where the liquid-metal flow was driven by the air compressor (FUJ-580A, Japan) and stabilized by the glue dispenser (MUSASHI MS-1, Japan). Each printing process lasted for 0.15 s when the nozzle was located at 15 mm above the elastomer surface and the air pressure was set at 0.2 MPa. The EGaIn droplets were also printed over the copper wires on the elastomer surface to secure a stable contact between the copper wires and electrode plates. It is noted that the EGaIn electrodes cannot sustain shear deformations due to the liquid property, so the Euler beam theory is valid to model the sensor with pure bending deformations.

The mold base was then assembled with cover B to form a mold container for casting the dielectric layer. The highly viscous solution was poured into the mold containers at a speed slow enough to evacuate the inside air through the gas ports on the cover. After 10 min when the solution started to cure, the mold was held in the horizontal position so that the newly cured dielectric layer was rigidly tied to the previous one. After removing the cover B, the wire B was attached and another EGaIn plate was printed on the dielectric layer. Then, the sealing layer was cured in the assembly of the cover C and mold base, after which the sensing module was released from the mold base. Each polyurethane elastomer layers were cured at 25°C for 3 h in the wax molds. The release agent (Mann-Ease Release 200, USA) was sprayed on the inner surfaces of each container to facilitate the release of elastomer from each mold.

Both end boxes were made of photosensitive resin with 3D printing, where the fixed-end box housed the circuit board and the copper wires were welded to connect the sensing module to the circuit board. The capacitance data were collected by the digitizer (Analog AD7746) with a high resolution up to 21 bits, whose sensing range of ± 4 pF could be extended to 0–21 pF by connecting a constant capacitor in serial. The main processor STM32F103 transmitted the measured data in multiple channels using the controller area network protocol at the sampling rate of 90 Hz.⁵⁴ The sensor was positioned on a human body by a hook-and-loop fastener on the fixed end. In the aforementioned process, the circuit board was waterproofed with Ecoflex sealing. The sensing module was encapsulated by the polyurethane elastomer, which not only provided the flexible structure with a good waterproof property but also prevented oxidization of the internal liquid metal plates.

Sensor Calibration and Characterization

Experiments were conducted to calibrate the flexible sensor and examine its dynamic characteristics, where the sensing module dimensions are listed in Table 1. Although the coefficients a and b in the formulated sensing model [Equation (9)] can be estimated by the sensor dimensions and material property, they are calibrated in the experiment as shown in Figure 3a, where one end was rigidly fixed and the other end was rotated by pulling a string with a micrometer. The rotation angles of static deformations were measured relative to the undeformed configuration with a protractor for calibration and the sensing results were compared with machine vision in both static and dynamic cases for error analysis. To investigate the water pressure effect on capacitive sensing, one

TABLE 1. DIMENSIONS OF SENSING MODULE

	<i>Length</i>	<i>Width</i>	<i>Height</i>
Effective sensing module	$L=15$	$W=10$	$D=5$
Upper electrode A	$l_1=12$	$w_1=5$	$z_1=1$
Lower electrode B	$l_2=13$	$w_2=6$	$z_2=1.5$
Distance between two electrodes			$d=0.5$

Unit: mm.

sensor prototype was put at the bottom of an iron tank of 40 cm depth, and the measured capacitance data were transmitted through a waterproof cable through the tank cover. The hydraulic pressure, increased by pumping water in the tank, was monitored by a pressure gauge as shown in Figure 3b.

Figure 3c plots the quadratic relation between C/C_0 and θ with the calibrated coefficients $a=9.88 \times 10^{-6}$ and $b=5.54 \times 10^{-4}$ where the correlation factor $R^2=0.9991$. When θ increased from 0° to 90° with the step size of 15° that was measured by a protractor, the capacitance was recorded at quasi-static states each of which was held for 10 s. This procedure was repeated for five times, and the measured results were averaged to obtain the calibrating capacitance. The same test was performed at 40 cm depth under water, where the deformed shape was incrementally changed and maintained by a fixing knot on the pulling string. Although the undeformed capacitance beneath the water surface becomes 0.8 pF smaller than its referenced value $C_0=13$ pF (measured at $\theta=0^\circ$ in the air without bending), the underwater measurements still conform to the calibrated model with a high precision ($R^2=0.9986$) because the capacitance varies proportionally. The aforementioned experimental result validates the functional form of Equation (9) and calibrates the coefficients in the sensing model.

To investigate the water pressure effect on the unbent sensor, the capacitance deviation δC_0 from C_0 was recorded with increasing the hydraulic pressure. Figure 3d shows that δC_0 increases almost linearly with the hydraulic pressure that is equivalent to the increasing depth under water. The maximum applied pressure of 0.6 MPa is equivalent to the pressure about 60 m depth under water. Given the small deviation of δC_0 compared with C_0 , the effect of hydraulic pressure on angle measurements can be neglected and the calibrated model is valid for human motion monitoring on land and under water.

To investigate the precisions in both static and dynamic sensing, the rotation angles measured by the flexible sensor were compared with those captured with machine vision. In the static case, the sensor was bent with the pulling string, and Figure 3e shows that the absolute error is <1.2° for 12 random measurements of rotation angles within 0° < θ < 100°. In the dynamic case, the sensor was continuously bent and relieved by an electric motor, and Figure 3f shows that the absolute average error is 0.582° and the maximum absolute error is 2.4966°. The aforementioned results quantify the precisions of the flexible sensor for both static and dynamic measurements.

The loading and unloading curves are plotted in Figure 3g to illustrate that the sensor has little hysteresis in bending deformations. The fatigue property was tested by monitoring the sensor capacitance for 5 h when bending of the same amplitude was applied for 2000 times on land and under water. The result in Figure 3h verifies that the sensor has a

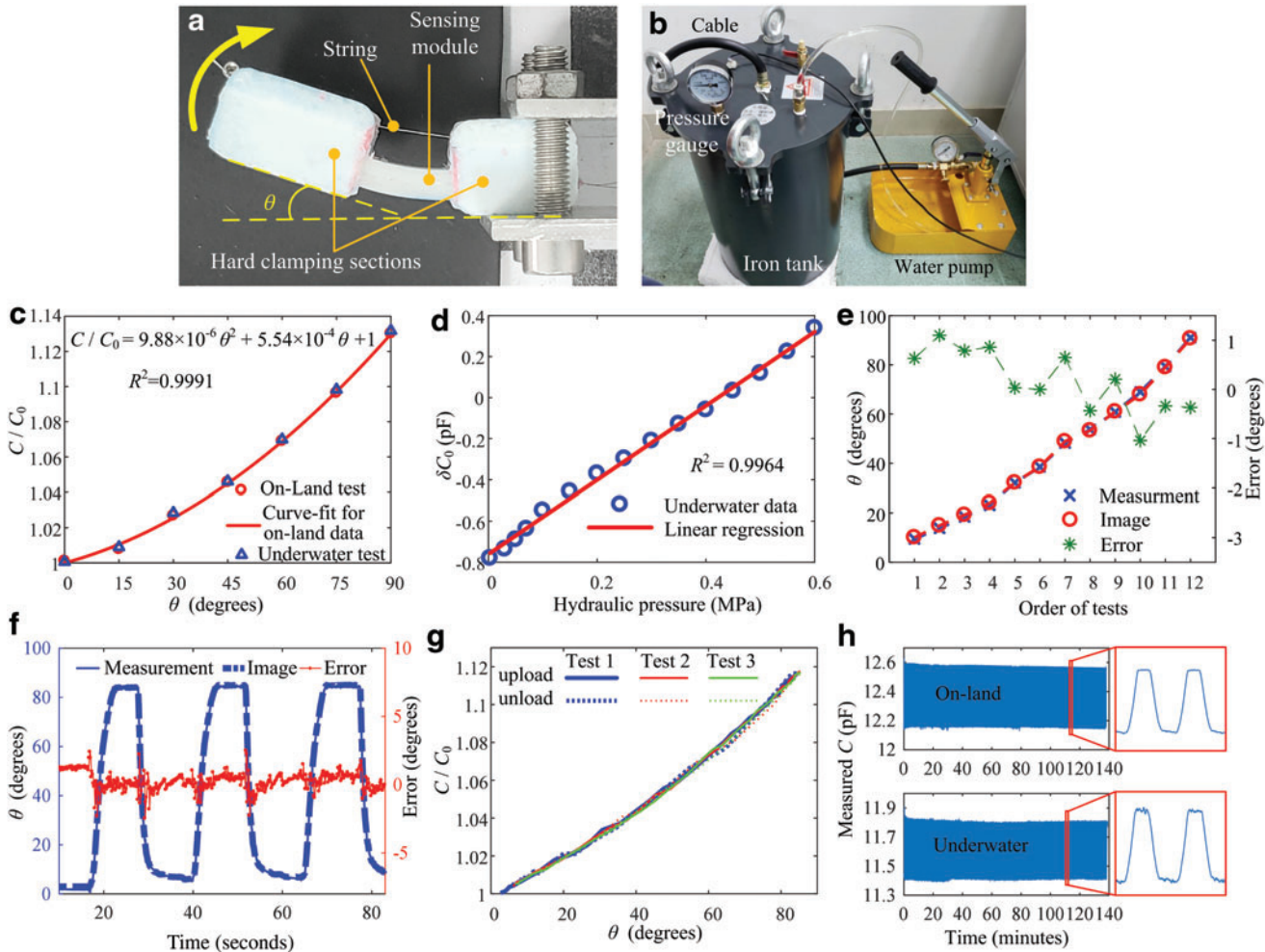


FIG. 3. Calibration and performance of a single flexible curvature sensor. **(a)** Experimental setup for sensor calibration. **(b)** Experimental setup for underwater investigation. **(c)** Calibrated relation between the relative capacitance change and applied bending angle of the sensor on land and under water. **(d)** Effect of hydraulic pressure on the initial capacitance of the sensor. **(e)** Sensing error in static measurements. **(f)** Sensing error in dynamic measurements. **(g)** Cyclic loading and unloading. **(h)** Cyclic bending from 0° to 90° for 2000 times on land and 2000 times under water. Color images are available online.

stable performance and is sustainable for long-period repetitive uses in amphibious environments.

Amphibious Gait Monitoring

Since the on-land and underwater experiments were performed at different time and different sites, the flexible sensor has to be doffed and donned again between sequential tests. In this way, manual installation of the sensor would incur an unpredictable but limited error, so the calibrated sensing model is first validated by a commercial motion capture system to quantitatively evaluate the installation error. It is noted that the sensor measurements have been calibrated relative to the undeformed sensor configuration and the unpredicted installation state can be captured with the initial measurement; this sensing model does not need recalibration as long as the sliding-end design guarantees pure bending of the sensing module. Then the same calibrated model is used for amphibious gait monitoring to validate the proposed design and sensing model that can compensate for the manual installation error in practice.

Validation with motion capture system

To demonstrate the application of the flexible capacitive sensor for human motion monitoring, the measured joint angles were compared against the commercial motion capture system (VICON F20-6, United Kingdom) using eight passive retroreflective markers and eight infrared cameras. The optical system was calibrated using the standard passive T-type wand, where the calibration matrix was automatically calculated with the Cortex software. The eight retroreflective markers were placed on the participant at the lateral calf, medial malleolus, heel, and toe on each side. Then the ankle rotation was characterized by the angle between the line connecting the lateral calf and medial malleolus markers and the line connecting the heel and toe markers whose positions were projected on the sagittal plane. For the comparison purpose, the measured angle with the flexible sensor needs to be transformed into the joint angle defined in the Vicon system.

As shown in Figure 4a, the sensor is tied to a diving boot with bandages where the sensing module is fixed on the shank through a nylon hook-and-loop fastener, and the sensor is

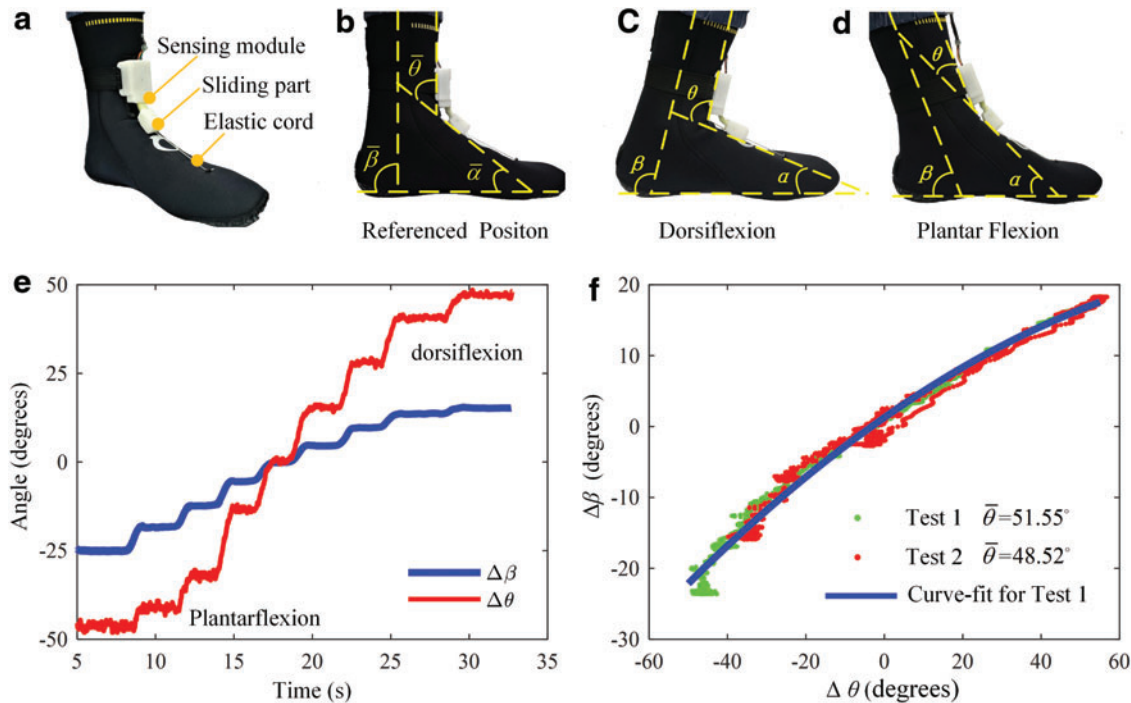


FIG. 4. Relation between sensor measurement and human joint rotation. (a) Sensor installation. (b) Reference state of ankle joint. (c) Dorsiflexion of ankle joint. (d) Plantar flexion of ankle joint. (e) Measured results of $\Delta\beta$ and $\Delta\theta$ in one test. (f) Comparison of relations between $\Delta\beta$ and $\Delta\theta$ in different tests, and a quadratic curve-fit between $\Delta\beta$ and $\Delta\theta$ for the first test. Color images are available online.

deformed by the sliding part as the ankle rotates. To maintain the sliding direction in the sagittal plane, a prestretched elastic cord passes through the sliding part and secures it on the instep surface with both cord ends sewn on the boot. The sensing configuration is illustrated in Figure 4b–d, where α is the angle between the instep and sole surfaces, and β is the angle between the shank and the sole. Based on the skeleton kinematics, the ankle rotation is relative to the standing state ($\bar{\beta}, \bar{\theta}$) when the shank is perpendicular to the sole as shown in Figure 4b. The standing state is chosen as the protocol in implementing the sensor because it is easy to characterize in practice and common in the start of various locomotion. In this way, the rotation angle of the ankle joint to be captured by the flexible sensor is presented as the deviation $\Delta\theta$ ($=\theta-\bar{\theta}$) whose positive and negative values correspond to ankle dorsiflexion and plantar flexion as shown in Figures 4c and 4d, respectively. Similarly, $\Delta\beta$ ($=\beta-\bar{\beta}$) is the rotation angle measured by the motion capture system, and $\Delta\alpha$ ($=\alpha-\bar{\alpha}$) characterizes musculoskeletal deformations of the foot instep and sole. Considering $\beta=\alpha+\theta$ and $\bar{\beta}=\bar{\alpha}+\bar{\theta}$, the following relation can be obtained:

$$\Delta\beta = \Delta\alpha + \Delta\theta. \quad (10)$$

Since the measured angles β and θ are defined in different ways as shown in Figures 4c and 4d, the rotation angles ($\Delta\beta, \Delta\theta$) need to be related to an approximated function that provides the interpolating values, so that the sensor measurements can be quantitatively compared with those from the motion capture system in the walking tests. Figure 4e shows the angles $\Delta\beta$ and $\Delta\theta$ when the ankle rotated from

plantar flexion to dorsiflexion. The same process was repeated for two times with the sensor being manually doffed and donned for an unpredicted change in the installation position. The measured results of $\Delta\beta$ and $\Delta\theta$ in both tests are superimposed in Figure 4f. The quadratic curve-fit between $\Delta\beta$ and $\Delta\theta$ for the first test ($\bar{\theta}=51.55^\circ$) is obtained as

$$\Delta\beta = -0.0016(\Delta\theta)^2 + 0.3865\Delta\theta + 1.275, \quad (11)$$

which is also valid for the second test ($\bar{\theta}=48.52^\circ$). It is noted that the measured $\Delta\beta$ and $\Delta\theta$ in two independent tests conform to the same relation [Equation (11)], because the error due to manual installation has been compensated by the initial sensor deflection $\bar{\theta}$, which is calculated as the positive solution to Equation (9) with \bar{C} measured initially at sensor installation.

Illustration with on-land walking

Application of the flexible capacitive sensing method is illustrated by monitoring ankle rotations in the sagittal plane. Five different walking gaits have been performed on a treadmill, including horizontal walking at different speeds (0.7, 0.9, and 1.1 m/s), ascending and descending at 0.9 m/s with the slope of 8°, where each test lasted for 90 s. Measured capacitance data were smoothed and filtered before they were used to calculate the ankle joint angle. Figure 5 compares the joint rotation angles measured by the flexible sensor against those obtained with the motion capture system. It was observed that there was about 30 ms delay in the flexible sensor signal compared with the motion capture system due

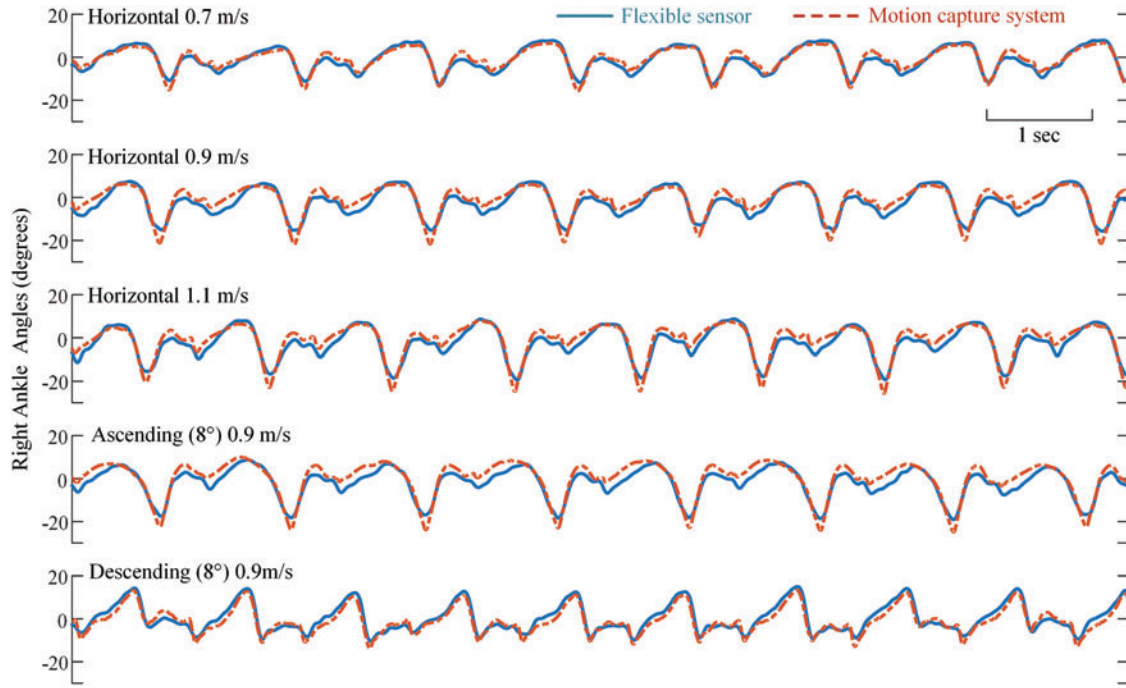


FIG. 5. Rotation angle of the *right* ankle was measured by the flexible sensor (*solid lines*) and the optical sensing system (*dotted lines*) for five different walking gaits where a 10-s period of data is presented for each test. Color images are available online.

to different data acquisition systems, and the delay was compensated for data synchronization in signal processing. It is noted that the 30 ms delay is still acceptable for real-time monitoring of general human motions. Table 2 presents the RMS errors of the flexible sensor results compared with the optical sensing data, where the maximum RMS errors for horizontal and descending walking are $<3^\circ$ and that for ascending motions are $<5^\circ$. It is observed that the RMS error tends to increase with the walking speed in the horizontal case, and the error for ascending is larger than those in the other two cases, which could be due to dynamic coupling of the flexible sensor and the human ankle joint.

Two independent tests were carried out on the ankle joint with the flexible sensor being doffed and donned, and the initial deflection angle $\bar{\theta}$ is 51.55° for Test 1 and 48.52° for Test 2. In both tests, the same calibrated relation of Equation (9) is employed as depicted in Figure 3c. Although the manual installation could incur a noise of 3.03° at the initial state, the absolute difference between the RMS errors in each case are much smaller than the installation error (Table 2),

because the installation effect on the sensing precision has been compensated by $\bar{\theta}$ evaluated with the operating capacitance \bar{C} in the sensing model formulation. The aforementioned analysis indicates that the calibrated sensing model [Equation (9)] is robust to the unpredictable manual installation error and it has an acceptable precision for joint motion measurements. Herein, one-time calibration becomes valid for repetitive uses whenever the flexible sensor is manually doffed and donned again to a human body.

Illustrative example of swimming

Application of the flexible sensor to underwater measurements was illustrated by method validation with optical sensing and ankle joint monitoring for two swimming gaits, where the same calibrated sensing model has been consistently used throughout the tests. To validate the flexible capacitive sensing in the underwater environment, a customized optical motion capture platform has been established as shown in Figure 6a. Four light-emitting diode (LED) markers

TABLE 2. ROOT-MEAN-SQUARE ERRORS OF MEASUREMENTS FOR FIVE MOTIONS

RMS error (degrees)	Horizontal 0.7 m/s	Horizontal 0.9 m/s	Horizontal 1.1 m/s	Ascent (8°) 0.9 m/s	Descent (8°) 0.9 m/s
Test 1	1.6739	2.6700	2.6448	3.2803	2.2921
Test 2	2.3251	2.5674	2.5757	4.5593	1.8181
Difference	0.6512	0.1026	0.0691	1.279	0.4740

RMS, root-mean-square.

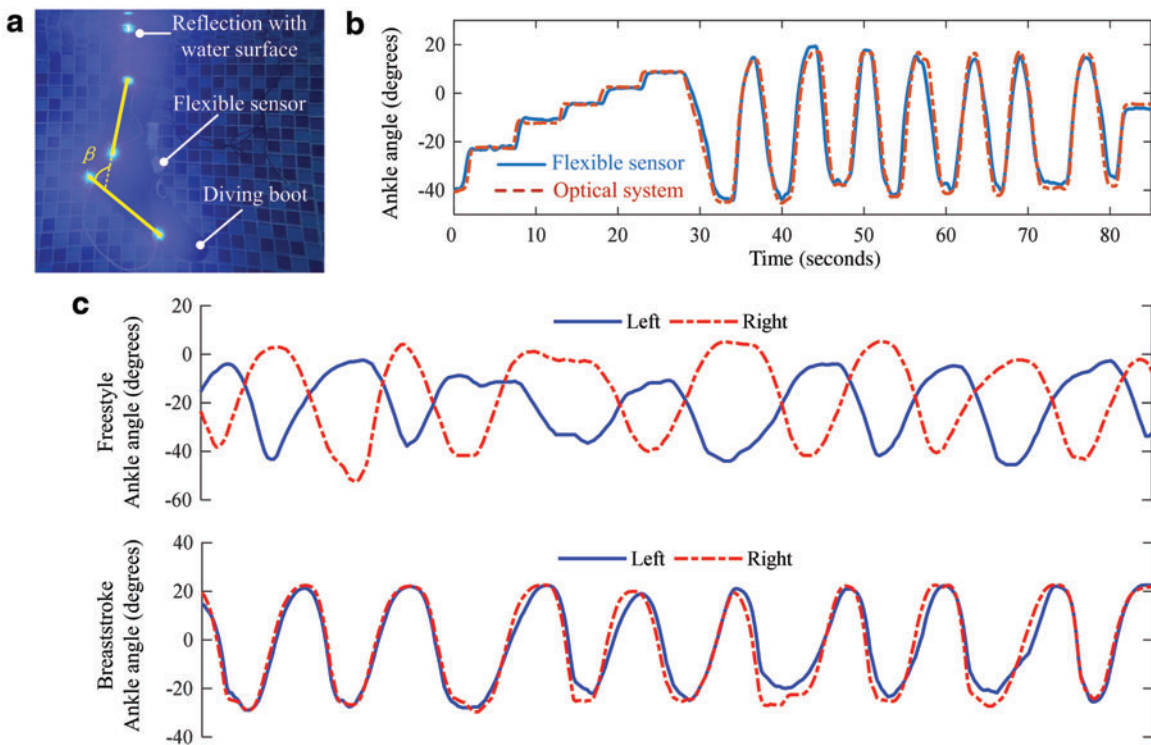


FIG. 6. Illustrative example of underwater application. (a) Experiment setup for underwater measurements. (b) Measurement comparison of the flexible sensor and optical motion capture system (Supplementary Video S2). (c) The flexible sensor measurements for freestyle and breaststroke swimming gaits (Supplementary Video S3). Color images are available online.

were implemented on the diving boot as references to the shank and sole, and their spatial positions were recorded with a waterproof camera (GoPro Hero6) whose lens-axis is normal to the ankle sagittal plane. Plantar flexion and dorsiflexion of an ankle joint were captured in quasi-static and periodic motions. Figure 6b compares the results from the flexible sensor with the optical measurements (see Supplementary Video S2), where the maximum absolute difference is 3° for the quasi-static states and 3.4° at the peaks in the periodic motion. Two gaits of freestyle and breaststroke swimming were measured, and Figure 6c compares the left and right ankle joint motions, in which the two joint angles are out of phase for the freestyle and in phase for the breaststroke (Supplementary Video S3). Although the motion amplitudes for both joints are similar in the breaststroke, the right joint rotation in the freestyle appears to be larger than the left counterpart probably due to personal preference of the participant who is right handed.

Conclusions

This article has developed a flexible capacitive sensor to measure human joint motions for amphibious applications. The sensor structure is fabricated using polyurethane elastomer through SDM and the capacitive electrode plates are printed with the EGaIn liquid metal. The electronic components are properly encapsulated and sealed with Ecoflex for the waterproof purpose. The sensing model is formulated with the flexible beam theory where the bending angle is related to the relative capacitance change through the deformed beam curvature. Calibrated with machine vision, the sensing model is valid to compensate for the manual

installation error when the sensor is doffed and donned to a human body for repetitive uses. With experimental validation using the motion capture system, it is shown that the RMS errors of the flexible sensor results are $<3^\circ$ for horizontal and descending walking and $<5^\circ$ for ascending motions. The application to amphibious gait monitoring has been illustrated with ankle motion measurement for walking on land and swimming under water, where the same calibrated sensing model of the flexible sensor has been consistently used throughout the tests. Although one-time sensor calibration is presented by accounting for the dominant effect of manual installation on repetitive uses of flexible sensors there are rooms for further studies and improvements, particularly on sensor reliability and robustness, for effective real-world implementations.

Author Disclosure Statement

No competing financial interests exist.

Funding Information

This research was supported by the National Natural Science Foundation of China (Grants 51875221, 51505164, U1713204, 91648203, and U1913601).

Supplementary Material

Supplementary Movie S1

Supplementary Movie S2

Supplementary Movie S3

References

1. Atalay A, Sanchez V, Atalay O, et al. Batch fabrication of customizable silicone-textile composite capacitive strain sensors for human motion tracking. *Adv Mater Technol* 2017;2:1700136.
2. Cai G, Wang J, Qian K, et al. Extremely stretchable strain sensors based on conductive self-healing dynamic cross-links hydrogels for human-motion detection. *Adv Sci* 2017; 4:1600190.
3. Cai L, Song L, Luan P, et al. Super-stretchable, transparent carbon nanotube-based capacitive strain sensors for human motion detection. *Sci Rep* 2013;3:3048.
4. Hwang B-U, Lee J-H, Trung TQ, et al. Transparent stretchable self-powered patchable sensor platform with ultrasensitive recognition of human activities. *ACS Nano* 2015;9:8801–8810.
5. Jarrett C, Mcdaid A. Modelling and feasibility of an elastomer-based series elastic actuator as a haptic interaction sensor for exoskeletons. *IEEE/ASME Trans Mechatron* 2019;24:1325–1333.
6. Lai YC, Hsiao YC, Wu HM, et al. Waterproof fabric-based multifunctional triboelectric nanogenerator for universally harvesting energy from raindrops, wind, and human motions and as self-powered sensors. *Adv Sci* 2019;6:1801883.
7. Trung TQ, Lee NE. Flexible and stretchable physical sensor integrated platforms for wearable human-activity monitoring and personal healthcare. *Adv Mater* 2016;28: 4338–4372.
8. Wang Y, Wang L, Yang T, et al. Wearable and highly sensitive graphene strain sensors for human motion monitoring. *Adv Funct Mater* 2014;24:4666–4670.
9. Yamada T, Hayamizu Y, Yamamoto Y, et al. A stretchable carbon nanotube strain sensor for human-motion detection. *Nat Nanotechnol* 2011;6:296.
10. Zhou H, Hu H. Human motion tracking for rehabilitation—a survey. *Biomed Signal Process Control* 2008;3:1–18.
11. Ahmed A, Zhang S L, Hassan I, et al. A washable, stretchable, and self-powered human-machine interfacing Triboelectric nanogenerator for wireless communications and soft robotics pressure sensor arrays. *Extreme Mech Lett* 2017;13:25–35.
12. Mcevoy MA, Correll N. Materials that couple sensing, actuation, computation, and communication. *Science* 2015; 347:1261689.
13. Ozel S, Keskin N A, Khea D, et al. A precise embedded curvature sensor module for soft-bodied robots. *Sens Actuators A* 2015;236:349–356.
14. Lim S, Son D, Kim J, et al. Transparent and stretchable interactive human machine interface based on patterned graphene heterostructures. *Adv Funct Mater* 2015;25:375–383.
15. Roh E, Hwang B-U, Kim D, et al. Stretchable, transparent, ultrasensitive, and patchable strain sensor for human-machine interfaces comprising a nanohybrid of carbon nanotubes and conductive elastomers. *ACS Nano* 2015;9: 6252–6261.
16. Amjadi M, Kyung K U, Park I, et al. Stretchable, skin-mountable, and wearable strain sensors and their potential applications: a review. *Adv Funct Mater* 2016;26:1678–1698.
17. Patel S, Park H, Bonato P, et al. A review of wearable sensors and systems with application in rehabilitation. *J NeuroEng Rehabil* 2012;9:21.
18. Rodgers MM, Pai VM, Conroy RS. Recent advances in wearable sensors for health monitoring. *IEEE Sens J* 2014; 15:3119–3126.
19. Legnani G, Zappa B, Casolo F, et al. A model of an electrogoniometer and its calibration for biomechanical applications. *Med Eng Phys* 2000;22:711–722.
20. Franchi M V, Longo S, Mallinson J, et al. Muscle thickness correlates to muscle cross-sectional area in the assessment of strength training-induced hypertrophy. *Scand J Med Sci Sports* 2018;28:846–853.
21. Mengüç Y, Park Y-L, Pei H, et al. Wearable soft sensing suit for human gait measurement. *Int J Robot Res* 2014;33: 1748–1764.
22. Guo J, Wang Z, Fu J, et al. Articular geometry reconstruction for knee joint with a wearable compliant device. *Robotica* 2019;37:2104–2118.
23. Xu K, Lu Y, Takei K. Multifunctional skin-inspired flexible sensor systems for wearable electronics. *Adv Mater Technol* 2019;4.
24. Jeong S H, Zhang S, Hjort K, et al. PDMS-based elastomer tuned soft, stretchable, and sticky for epidermal electronics. *Adv Mater* 2016;28:5830–5836.
25. Amjadi M, Yoon YJ, Park I. Ultra-stretchable and skin-mountable strain sensors using carbon nanotubes–Ecoflex nanocomposites. *Nanotechnology* 2015;26:375501.
26. Majidi C, Kramer R, Wood R. A non-differential elastomer curvature sensor for softer-than-skin electronics. *Smart Mater Struct* 2011;20:105017.
27. Liu H, Zhao H, Li S, et al. Adhesion-free thin-film-like curvature sensors integrated on flexible and wearable electronics for monitoring bending of joints and various body gestures. *Adv Mater Technol* 2019;4:1800327.
28. Amjadi M, Pichitpajongkit A, Lee S, et al. Highly stretchable and sensitive strain sensor based on silver nanowire-elastomer nanocomposite. *ACS Nano* 2014;8:5154–5163.
29. Gong S, Lai D T, Wang Y, et al. Tattoo-like polyaniline microparticle-doped gold nanowire patches as highly durable wearable sensors. *ACS Appl Mater Interfaces* 2015;7: 19700–19708.
30. Han C-J, Chiang H-P, Cheng Y-C. Using micro-molding and stamping to fabricate conductive polydimethylsiloxane-based flexible high-sensitivity strain gauges. *Sensors* 2018; 18:618.
31. Jeong D-W, Jang N-S, Kim K-H, et al. A stretchable sensor platform based on simple and scalable lift-off micro-patterning of metal nanowire network. *RSC Adv* 2016;6: 74418–74425.
32. Jeong YR, Park H, Jin SW, et al. Highly stretchable and sensitive strain sensors using fragmentized graphene foam. *Adv Funct Mater* 2015;25:4228–4236.
33. Kang D, Pikhitsa PV, Choi YW, et al. Ultrasensitive mechanical crack-based sensor inspired by the spider sensory system. *Nature* 2014;516:222.
34. Li X, Zhang R, Yu W, et al. Stretchable and highly sensitive graphene-on-polymer strain sensors. *Sci Rep* 2012;2: 870.
35. Liu C-X, Choi J-W. Analyzing resistance response of embedded PDMS and carbon nanotubes composite under tensile strain. *Microelectron Eng* 2014;117:1–7.
36. Lu N, Lu C, Yang S, et al. Highly sensitive skin-mountable strain gauges based entirely on elastomers. *Adv Funct Mater* 2012;22:4044–4050.
37. Mattmann C, Clemens F, Tröster G. Sensor for measuring strain in textile. *Sensors* 2008;8:3719–3732.

38. Muth JT, Vogt DM, Truby RL, *et al.* Embedded 3D printing of strain sensors within highly stretchable elastomers. *Adv Mater* 2014;26:6307–6312.
39. Park Y-L, Chen B-R, Pérez-Arcibia NO, *et al.* Design and control of a bio-inspired soft wearable robotic device for ankle-foot rehabilitation. *Bioinspiration Biomimetics* 2014;9:016007.
40. Shin U-H, Jeong D-W, Park S-M, *et al.* Highly stretchable conductors and piezocapacitive strain gauges based on simple contact-transfer patterning of carbon nanotube forests. *Carbon* 2014;80:396–404.
41. Cohen D J, Mitra D, Peterson K, *et al.* A highly elastic, capacitive strain gauge based on percolating nanotube networks. *Nano Lett* 2012;12:1821–1825.
42. Fassler A, Majidi C. Soft-matter capacitors and inductors for hyperelastic strain sensing and stretchable electronics. *Smart Mater Struct* 2013;22:055023.
43. Frutiger A, Muth JT, Vogt DM, *et al.* Capacitive soft strain sensors via multicore–shell fiber printing. *Adv Mater* 2015; 27:2440–2446.
44. Lipomi DJ, Vosgueritchian M, Tee BC, *et al.* Skin-like pressure and strain sensors based on transparent elastic films of carbon nanotubes. *Nat Nanotechnol* 2011;6:788.
45. Yao S, Zhu Y. Wearable multifunctional sensors using printed stretchable conductors made of silver nanowires. *Nanoscale* 2014;6:2345–2352.
46. Gu G, Xu H, Peng S, *et al.* Integrated soft ionotronic skin with stretchable and transparent hydrogel-elastomer ionic sensors for hand-motion monitoring. *Soft Robot* 2019;6: 368–376.
47. Tairych A, Anderson IA. Capacitive stretch sensing for robotic skins. *Soft Robot* 2019;6:389–398.
48. Hu W, Niu X, Zhao R, *et al.* Elastomeric transparent capacitive sensors based on an interpenetrating composite of silver nanowires and polyurethane. *Appl Phys Lett* 2013; 102:38.
49. Wu J, Tang SY, Fang T, *et al.* A wheeled robot driven by a liquid-metal droplet. *Adv Mater* 2018;30:1805039.
50. Hong SK, Yang S, Cho SJ, *et al.* Development of a waterproof crack-based stretchable strain sensor based on PDMS shielding. *Sensors* 2018;18:1171.
51. Larson C, Sjput J, Knepper R, *et al.* A deformable interface for human touch recognition using stretchable carbon nanotube dielectric elastomer sensors and deep neural networks. *Soft Robot* 2019;6:611–620.
52. Lin S, Zhao X, Jiang X, *et al.* Highly stretchable, adaptable, and durable strain sensing based on a bioinspired dynamically cross-linked graphene/polymer composite. *Small* 2019;15:e1900848.
53. Guo J, Lee K-M, Zhu D, *et al.* Large-deformation analysis and experimental validation of a flexure-based mobile sensor node. *IEEE/ASME Trans Mechatron* 2012;17:606–616.
54. Ma X, Guo J, Lee K-M, *et al.* A soft capacitive wearable sensing system for lower-limb motion monitoring. In: 12th International Conference of Intelligent Robotics and Applications, Shenyang, China, ICIRA, August 8–11, 2019, pp. 467–479.

Address correspondence to:

Jiajie Guo

State Key Laboratory of Digital
Manufacturing Equipment and Technology
School of Mechanical Science and Engineering
Huazhong University of Science and Technology
1037 Luoyu Rd.

Wuhan 430074, Hubei
China

E-mail: jiajie.guo@hust.edu.cn